IEEE Access
Multidisciplinary | Rapid Review | Open Access Journal

Received 22 October 2023, accepted 16 November 2023, date of publication 23 November 2023,
date of current version 1 December 2023.

Digital Object Identifier 10.1109/ACCESS.2023.3336308

RESEARCH ARTICLE

Lower Limb Exoskeleton With Energy-Storing Mechanism for Spinal Cord Injury Rehabilitation

BRANESH M. PILLAI[1], (Member, IEEE), PEERAPAT OWATCHAIYAPONG[2], SHEN TRERATANAKULCHAI[1], (Member, IEEE), DILEEP SIVARAMAN[1], (Graduate Student Member, IEEE), SONGPOL ONGWATTANAKUL[1], (Member, IEEE), AND JACKRIT SUTHAKORN[1], (Member, IEEE)

[1]Center for Biomedical and Robotics Technology (BART LAB), Faculty of Engineering, Mahidol University, Nakorn Pathom 73170, Thailand
[2]Department of Mechanical Engineering, Faculty of Industrial Education, Rajamangala University of Technology Phra Nakhon, Bangkok 10300, Thailand

Corresponding author: Jackrit Suthakorn (jackrit.sut@mahidol.ac.th)

This work was supported by the Drug and Medical Supplies Delivery Mobile Robotic System through Mahidol University (Grant No. 60440) and Reinventing System through Mahidol University, Mahidol Medical Robotics Platform (IO 864102063000).

ABSTRACT Statistics from the National Office for Empowerment of Persons with Disabilities (NEP) indicate that Spinal Cord Injury (SCI) is a major cause of disability in the Thai population. Various rehabilitation methods are available to support SCI patients. Assistive robots, such as exoskeletons and prosthetics, are very useful for improving quality of life. Robotic exoskeletons have evolved as rehabilitation methods that can overcome some of the current health-related effects of SCI. In the current study, a lower-limb exoskeleton was developed to assist or rehabilitate a physically challenged person who has lost mobility owing to SCI. To overcome energy storage issues related to existing designs, the device uses a spring and camshaft system that is integrated with the robot structure to reduce the required energy by absorbing the body weight into spring potential energy and released by the cam design. Hence, the spring cam system significantly reduced torque on the joints, with approximately $17-30\%$ reduction in the angle joint and $40-48\%$ reduction in the knee joint. Control of the exoskeleton is carried out by analyzing brain signals (EEG) and eye movement signals (EOG), which are combined with the control system to perform daily activities, such as walking, turning, and standing. This exoskeleton boasts a maximum walking speed of 0.5 m/s and a remarkable two-hour full-load operation, making it a promising solution for enhancing the mobility and quality of life of individuals with SCI. The effectiveness of the developed exoskeleton in assisting individuals with mobility impairments was validated through comprehensive laboratory-level experimental analysis.

INDEX TERMS Spinal cord injury (SCI), robotic rehabilitation, lower limb exoskeleton, medical robotics, brain-computer interface, gait analysis, biomechanics.

I. INTRODUCTION

Mobility impairment resulting from spinal cord injury (SCI) significantly restricts an individual's ability to perform daily activities including walking, turning, and sitting/standing [1]. Paraplegic patients require mobility devices to help them move around in their environment, but they have different requirements according to the degree of disability. To retain their level of limb use and muscle fitness, patients with partial limb usability need assisted exercise; those with total disability need an alternative to their muscle strength so that they can work at a level equivalent to that of a person without such limitation. These patients need an assistive device that can provide independent mobility and

The associate editor coordinating the review of this manuscript and approving it for publication was Jingang Jiang.

help them function effectively in conditions that are not typical for patients with disabilities of the lower extremities. The traditional rehabilitation process is led by the therapist, whose primary goal is to provide basic skills, such as bed mobility, wheelchair management and transfers, caregiver training, rehabilitation equipment training, and basic medical education. However, the availability of therapists is limited, and treatment is expensive.

Robotic exoskeletons have emerged as a promising solution for assisting and rehabilitating patients with mobility impairments [2], [3], [4]. This paper presents a comprehensive study focused on the development of a brain signal-activated lower limb robotic exoskeleton tailored to meet the specific needs of paraplegic patients within the Thai population. Gait pattern design is a crucial aspect of this study, ensuring compatibility with the general dimensions and biomechanics of Thai individuals. To enhance the performance of the exoskeleton, a novel spring-cam-based variable-stiffness actuation system is integrated into the exoskeleton structure. This innovative system allows the storage of the required torque as elastic potential energy, enabling soft landing and efficient force dissipation during locomotion [5], [6]. Seamless interaction between the user and exoskeleton is achieved through the incorporation of brain signals (electroencephalography, EEG) and eye movement signals (electrooculography, EOG) into the control system, allowing for the comprehension of the user's intention and prediction of desired movements.

In addition to the advanced control system, this study also focuses on the biomechanical modeling of the human body within the exoskeleton framework. By considering the effects of reaction force and utilizing a comprehensive biomechanical model, system dynamics and stability are significantly enhanced, resulting in improved performance and safety during locomotion.

From this point of view, the BART LAB Lower Limb Exoskeleton (BART LAB LL-EXO-I) was developed by the Center for Biomedical and Robotics Technology (BART LAB), Mahidol University [7]. This study specifically addresses the issues faced by paraplegic patients with SCI at stage 3 and below the lumbar spinal cord. This wearable exoskeleton robot, with four degrees of freedom in each leg and one degree of freedom in the torso, was designed to assist in gait failure. The gait pattern was based on clinical gait analysis (CGA) using the David A Winter database, ensuring its compatibility with paraplegic patients' locomotion [8], [9].

Building on the success of BART LAB LL-EXO-I, this study presents the design and development of a brain-signal-activated robotic lower-limb exoskeleton (BART LAB EXO-II, as shown in Fig.1) aimed at assisting and rehabilitating mobility-impaired paraplegic patients with SCI. Data collected during various motions such as walking, sitting, standing, and turning were used to estimate the power requirements and were stored in a motion database. A comprehensive laboratory-level experimental analysis was conducted to validate the suitability of the exoskeleton for practical application and its effectiveness in assisting individuals with mobility impairments caused by SCI.

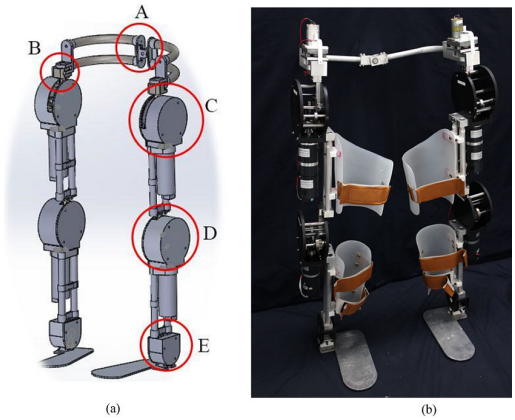

FIGURE 1. (a) Overall mechanical design and the Degree of Freedom: (A) shows the middle of the hip joint, (B) is the hip rotation joint, (C) is the hip flexion/extension joint, (D) shows knee flexion/extension joint and (E) is ankle flexion and inversion/eversion joint, (b) developed BART-LAB-EXO-II.

II. RELATED WORKS

This section is dedicated to surveying the existing body of knowledge, including innumerable efforts to develop an exoskeleton [10], [11], [12], [13], [14], [15], [16], [17] and notable review papers [18], [19], [20], to provide readers with a holistic understanding of the current state of research on the lower limb exoskeleton. These three review papers collectively contribute to the advanced literature review on research and development in the field of robotic lower-limb exoskeletons.

Young et al.'s [18] review provides an overview of the current state of the field and highlights the need for rigorous quantitative evaluations, whereas Plaza et al.'s [19] study offers valuable insights and suggestions for improving the current design of exoskeleton devices. Furthermore, Hybart and Ferris [20] proposal to utilize mobile brain imaging techniques for measuring embodiment during human-machine interactions demonstrated the importance of integrating quantitative measures in exoskeleton research. Together, these studies shed light on key aspects, such as design approaches, user interface, control, and embodiment, paving the way for the development of more effective and successful robotic lower-limb exoskeletons.

Aguirre-Ollinger et al. [21] presented a new method for controlling lower-limb exoskeletons to enhance the agility of the leg-swing motion by compensating for the inertia of the exoskeleton. Their findings highlighted the effectiveness of the proposed controller in increasing the natural frequency of the lower limbs and enabling net work per swing cycle, leading to improved agility and performance. This study provides valuable insights into optimizing the control mechanisms of exoskeletons.

Similarly, Xie et al. developed an unpowered flexible lower-limb exoskeleton [22] that assists human walking without external electrical power. Their approach leverages the harvesting of kinetic energy during lower limb deceleration to assist in acceleration movement, thereby reducing biomechanical power consumption during walking. In addition, the exoskeleton integrates a generator for self-sustainable power generation to support wearable electronics. The experimental results confirm the effectiveness of the flexible exoskeleton in reducing the metabolic cost of walking and generating electricity. This innovative solution addresses the limitations associated with bulky energy supply systems in powered exoskeletons and offers potential advancements in reducing metabolic costs and enabling self-sustainability.

These two studies explored novel approaches to exoskeleton control and energy efficiency. The research conducted by Gabriel et al. focused on enhancing control mechanisms to improve agility, while Longhan et al. addressed the challenge of energy supply in exoskeletons. In contrast, this study presents a comprehensive development of a brain signal-activated lower-limb robotic exoskeleton specifically tailored for paraplegic patients within the Thai population. The emphasis is on designing a gait pattern compatible with Thai individuals' dimensions and biomechanics, integrating a novel spring-cam-based variable-stiffness actuation system for efficient force dissipation, and incorporating brain and eye movement signals for seamless user-exoskeleton interaction. Furthermore, this study addresses biomechanical modeling, system dynamics, and stability to enhance performance and safety. This research extends the existing knowledge by focusing on the specific needs of paraplegic patients with spinal cord injuries and incorporating clinical gait analysis and validation through experimental analysis and motion database utilization.

III. MATERIALS AND METHODS

In the developed BART LAB EXO-II, the system was divided into five components: motion experiment and data analysis, ground reaction force, mechanical design, energy storage system, signal activator, and robot control system.

A. MOTION EXPERIMENT AND DATA ANALYSIS

Position data were collected using the 'Optitrack(R) s250e' (NaturalPoint, Inc. DBA OptiTrack Corvallis, OR) - camera motion capture system [23]. Tracking markers were strategically placed at key positions, including the trunk, hip, knee, ankle, heel, and metatarsal bone (toe) to accurately capture the movement of various joints during the experiment. Markers were attached on both sides of the leg was specifically done to capture turning motions more comprehensively. While joint angles can be measured by attaching markers at specified positions, the inclusion of markers on the toe joint is crucial for obtaining a complete motion profile and ensuring a comprehensive analysis of gait and movement patterns. The markers placed on the toe joint contribute to a more precise and holistic understanding of the subject's movements, particularly during dynamic activities, such as turning. This approach aligns with standard motion capture practices, allowing for robust data collection and reliable calculation of joint angles throughout the study (The experimental setup, as demonstrated in Fig. 2).

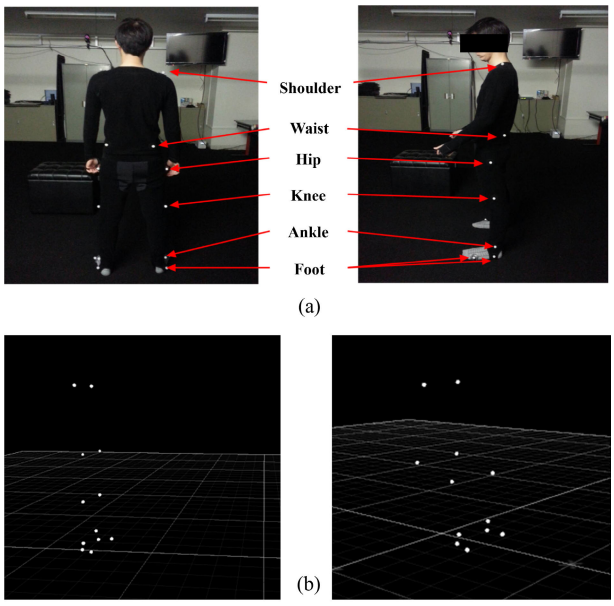

FIGURE 2. (a) Position data were collected using the 'Optitrack(R) s250e' camera motion capture system with strategically placed markers on key body positions, including the toe joint, to comprehensively capture joint movement during dynamic activities like turning. (b) Position of markers in both standing and sitting positions.

Incorporating normal gait patterns in the exoskeletons of patients with SCI is an essential aspect that should be explored. However, the robot's degrees of freedom (DoFs) may differ from those of an actual human, and we agree that additional considerations are crucial when designing exoskeletons for SCI patients. One significant consideration is the restricted range of motion in each joint due to stiffness, which is common in patients with SCIs.

For walking, a normal gait cycle, as described in [24] and [25], was considered. This cycle was divided into three distinct phases: starting, walking, and stopping, as illustrated in Fig. 3-(a). For the sit-stand and stand-sit motions, the patterns exhibited similarities. Hence, two separate experiments were conducted, one with arm support and the other without arm support, as shown in Fig. 3-(b).

Employing the OptiTrack S250e camera-based motion capture system, in conjunction with strategically positioned retro-reflective markers on anatomical landmarks, enabled the measurement of hip turning angles during dynamic movements (as shown in Fig. 2). System calibration and subject preparation preceded the meticulous recording of motion data as the participants executed the turning motions. Subsequently, the recorded data were processed using OptiTrack software, facilitating the precise tracking of marker positions that represented the hip joint locations over time. Analysis of marker orientation in relation to a reference axis

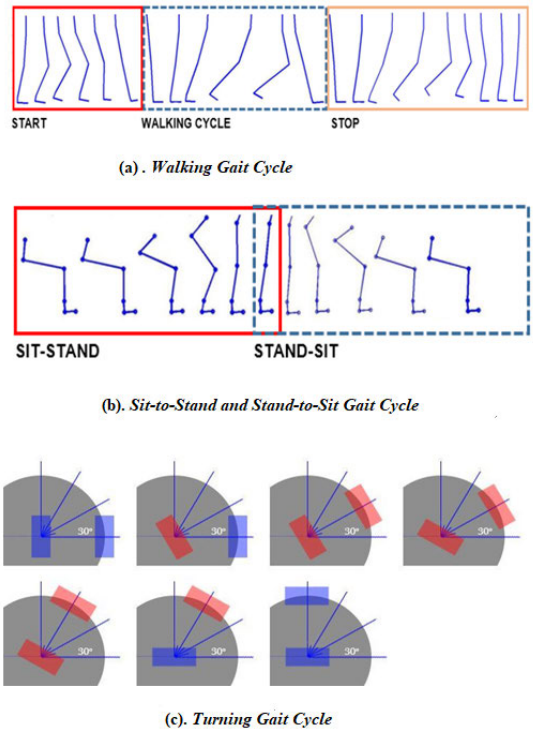

FIGURE 3. (a) Walking Gait Cycle, (b) Sit-to-Stand and Stand-to-Sit Gait Cycle, (c) Turning Gait Cycle.

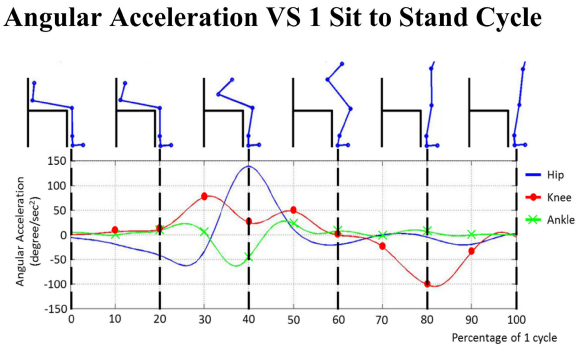

FIGURE 4. The required angular accelerations for sit-to-stand movement.

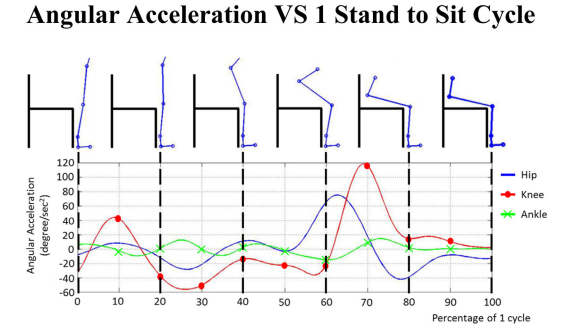

FIGURE 5. The required angular accelerations for stand-to-sit movement.

allowed for the calculation of hip-turning angles, yielding insights into hip joint movements throughout the turning cycle.

Turning motion poses intricate biomechanical and neuromuscular challenges [26]. The turning scheme is illustrated in Fig. 3-(c), involving three steps to complete one 90-degree turn, meaning each step encompasses 30 degrees of motion. Subsequently, data collection was followed by comprehensive computations to determine various parameters, including relative angles (degrees), angular velocity (rad/s), angular acceleration (rad/s^2), linear acceleration (m/s^2), and moment (Nm) during motion.

Additionally, we estimated the required angular accelerations for the sit-to-stand and stand-to-sit movements, as shown in Fig. 4 and 5, along with the required torque for the knee and ankle, as depicted in Fig. 6. These calculations and estimations are fundamental to understanding the dynamics of motion and are essential for designing exoskeletons that accommodate the biomechanical needs of individuals with SCI.

B. GROUND REACTION FORCE

To create exoskeletons and wearable assistive devices for lower-limb support, it is essential to estimate the Ground Reaction Force (GRF) from the foot to the surface [27], [28]. The estimation of GRFs using the 'MatScan(R)' (Tekscan, Inc. Norwood, United States) system plays a critical role in this study. First, it ensures balance and stability of the wearer, provides appropriate support, lowers the risk of falling, and preserves balance by precisely predicting the GRF. Second, understanding GRF is directly related to the loading placed on the hip, knee, and ankle joints. By efficiently balancing and optimizing these forces using an exoskeleton, the strain, pain, and potential injuries in these joints can be reduced.

Specific aspects of the exoskeleton, such as controlling the ankle joint actuator, incorporate the knowledge acquired about the GRF. We aim to utilize this information to facilitate natural walking or running movements, improve gait efficiency, and reduce the effort of the wearer during various parts of the gait cycle [29].

Furthermore, the precise prediction of the GRF has implications for the energy economy, which is a crucial factor in exoskeleton design. By optimizing the exoskeleton design and control based on the GRF data, we can enhance the wearer's energy efficiency by reducing energy loss and ensuring efficient power transmission.

The following equation can be used to represent the total force (related to the acceleration of the center of gravity (COG) as a result), GRF, and body weight numerically [30]:

$$F_{Gz} = Ma_z + Mg = M(a_z + g) \tag{1}$$

where M is the body mass, a is the acceleration of the body's center of mass, and g is the acceleration due to gravity. If $F_{Gz}[BW]$ is the z-component of the GRF normalized to the body weight, it can be measured in terms of acceleration.

$$F_{Gz}[BW] = \frac{a_z + g}{g} \tag{2}$$

To accurately calculate the GRF by analyzing the torques exerted on the hip, knee, and ankle joints, a comprehensive

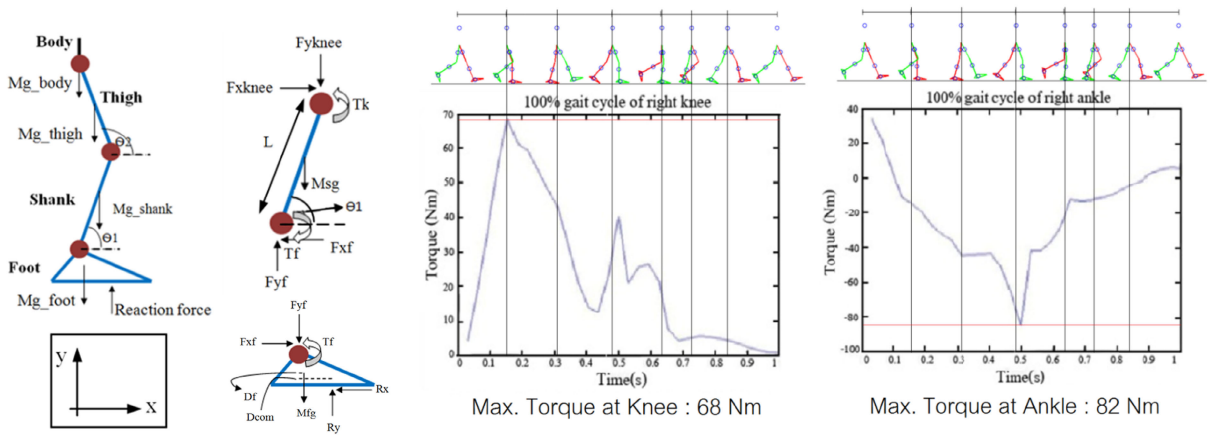

FIGURE 6. The required torque for the knee and ankle.

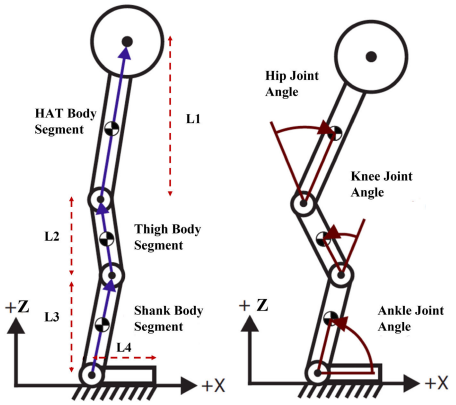

FIGURE 7. A human biomechanical model with hip, knee, and ankle joints and body segments for the head, upper body (HAT), thigh, and lower leg (shank) in two dimensions.

biomechanical model must consider various influencing factors. Although body weight and segment length are significant contributors to joint torques, it is essential to acknowledge that individual variations, such as muscle strength, joint stiffness, and joint angles, can also impact these torques. The biomechanical model encompasses the hip, knee, and ankle joints, along with the corresponding body segments for the head, upper body (HAT), thigh, and lower leg (shank) in 2-D, as depicted in Fig. 7. This model enables a more accurate estimation of GRFs during lower-limb movements by accounting for a broader range of factors beyond body weight and segment length, including gravitational force, leg segment masses, and joint angles. Understanding these complex interactions is essential for interpreting results and ensuring the practical applicability of the findings.

To calculate the torques involved in the sit-to-stand and standing-to-sit movements. The equations for each torque are as follows. From Fig. 7 the torque on each joint for sit-to-stand and stand-to-sit can be calculated using Equations 3, 4, 5, 6, 7, and 8.

1) HIP TORQUE

For the sitting position,

$$\tau_{hip-sit} = m_{body} \cdot g \cdot L(1) \cdot \cos(\theta_{sit}) \tag{3}$$

For the standing position,

$$\tau_{hip-stand} = m_{body} \cdot g \cdot L(1) \cdot \cos(\theta_{stand}) \tag{4}$$

2) KNEE TORQUE

For the sitting position,

$$\begin{aligned}\tau_{knee-sit} = {} & m_{leg}(2) \cdot L(2) \cdot (L(3) \cdot m_{leg}(3) \cdot g \cdot \cos(\theta_{sit}) \\ & + L(4) \cdot m_{leg}(3) \cdot g \cdot \cos(\theta_{sit}) \\ & - L(1) \cdot m_{body} \cdot g \cdot \cos(\theta_{sit}) \cdot \cos(\theta_{sit})) \end{aligned} \tag{5}$$

For the standing position,

$$\begin{aligned}\tau_{knee-stand} = {} & m_{leg}(2) \cdot L(2) \cdot (L(3) \cdot m_{leg}(3) \cdot g \cdot \cos(\theta_{stand}) \\ & + L(4) \cdot m_{leg}(3) \cdot g \cdot \cos(\theta_{stand}) \\ & - L(1) \cdot m_{body} \cdot g \cdot \cos(\theta_{stand}) \cdot \cos(\theta_{stand})) \end{aligned} \tag{6}$$

3) ANKLE TORQUE

For the sitting position,

$$\begin{aligned}\tau_{ankle-sit} = {} & m_{leg}(3) \cdot L(3) \cdot g \cdot \cos(\theta_{sit}) \\ & + m_{leg}(3) \cdot L(4) \cdot g \cdot \cos(\theta_{sit}) \\ & - m_{body} \cdot L(1) \cdot g \cdot \cos(\theta_{sit}) \cdot \cos(\theta_{sit}) \\ & - m_{leg}(2) \cdot L(2) \cdot g \cdot \cos(\theta_{sit}) \end{aligned} \tag{7}$$

For the standing position,

$$\begin{aligned}\tau_{ankle-stand} = {} & m_{leg}(3) \cdot L(3) \cdot g \cdot \cos(\theta_{stand}) \\ & + m_{leg}(3) \cdot L(4) \cdot g \cdot \cos(\theta_{stand}) \\ & - m_{body} \cdot L(1) \cdot g \cdot \cos(\theta_{stand}) \cdot \cos(\theta_{stand}) \\ & - m_{leg}(2) \cdot L(2) \cdot g \cdot \cos(\theta_{stand}) \end{aligned} \tag{8}$$

where $m_{leg}(1)$, $m_{leg}(2)$, and $m_{leg}(3)$ are the masses of each leg segment, and $L(1)$, $L(2)$, and $L(3)$ are the lengths of each leg segment. By utilizing the calculated torques, we further determined the reaction forces at the foot joint for both sitting and standing positions. The reaction forces were calculated as the difference between the gravitational force acting on the leg segment (specifically, the foot segment) and the torque generated at the ankle joint.

4) REACTION FORCE AT FOOT JOINT

For the sitting position,

$$F_{foot-sit} = m_{leg}(3) \cdot g - \tau_{ankle-sit} \tag{9}$$

For the standing position,

$$F_{foot-stand} = m_{leg}(3) \cdot g - \tau_{ankle-stand} \tag{10}$$

In these equations, the variables $F_{foot-sit}$ and $F_{foot-stand}$ represent the reaction forces at the foot joint for the sitting and standing positions, respectively. In addition to the reaction forces, estimating the coordinates of the foot joint to gain a comprehensive understanding of human biomechanics in sitting and standing positions. Using Equations (11) and (12), the coordinates were determined based on the angle (θ) and the length of the fourth body segment ($L(4)$).

For the sitting position,

$$\begin{aligned} x_{foot-sit} &= L(4) \cdot sin(\theta_{sit}) \\ y_{foot-sit} &= 0 \\ z_{foot-sit} &= -L(4) \cdot cos(\theta_{sit}) \end{aligned} \tag{11}$$

For the standing position,

$$\begin{aligned} x_{foot-stand} &= L(4) \cdot sin(\theta_{stand}) \\ y_{foot-stand} &= 0 \\ z_{foot-stand} &= -L(4) \cdot cos(\theta_{stand}) \end{aligned} \tag{12}$$

Analyzing sit-to-stand and stand-to-sit motions aims to gain essential insights into the biomechanics and kinetics of lower limb movements during these crucial transitional phases. Understanding the joint torques, GRFs, and the required angular accelerations in these motions is crucial for designing exoskeletons that can effectively assist individuals with mobility challenges during such functional activities [31].

Furthermore, focusing on these particular motions allowed us to target the specific challenges associated with transitioning between the sitting and standing postures. This analysis provides valuable data for developing exoskeletons that can optimize the required assistance and enhance the overall stability and safety of the wearer during these dynamic motions.

C. MECHANICAL DESIGN

The mechanical design of BART LAB EXO-II has a total of 11 degrees of freedom: five passive joints in the middle robot and other 4 joints at the ankle, and six active joints at the hip and knee. The middle joint of the hip allowed the legs to move in the coronal plane for abduction and adduction. This joint is a passive joint because during the walking cycle, sagittal plane movement is vital and movement in another plane should be supported for balance [32]. Therefore, the passivity of this joint assists the movement, which depends on the pose of the patient. Each leg has two degrees of freedom at the hip: rotation and flexion/extension. For rotation, motors were positioned to assist the turning process. The high-torque motor was vertically placed so that leg rotation was allowed without loss of power. For movement in the sagittal plane, the hip joint requires a range of motion from −20 degrees to 30 degrees from the normal alignment in walking but needs 90 degrees in sitting. Therefore, the total angle range of the hip was −20 degrees to 90 degrees. The motor shaft transfers motion through bevel gears to change the orientation of the movement. Knee joint movement is primarily in the sagittal plane; therefore, we use only one degree of freedom for the knee joint. The range of the angle of the knee while walking is from 0 degrees to 50 degrees but for sitting, is extended to 90 degrees.

The exoskeleton design incorporates knee joints that bear similarities to hip joints in their structural arrangement and basic kinematic principles [33], [34]. Actuation mechanisms are designed to mimic natural human movement patterns and provide support and assistance during lower-limb motions. Although some subtle differences exist in the actuators used, the overall mechanical configuration emphasizes a comparable approach to achieve functional and biomechanically appropriate movements. A similar mechanical configuration allows for a streamlined and cohesive exoskeleton design, supporting natural gait patterns, and enhancing user comfort. This approach optimizes the functionality of the exoskeleton and effectively supports coordinated lower-limb movements during walking, thereby benefiting individuals with mobility impairments. Fig. 8 and Fig. 9 provide a comprehensive depiction of the entire exoskeleton system, showing the integration of the various components.

The free-body diagram in Fig. 10 shows the force that occurs in each section of the leg. The BART LAB EXO-II exoskeleton incorporates a total of 11 degrees of freedom, including passive joints that support frontal plane movements. Although the kinematic model appears simplified in the illustration, the design philosophy encompasses a broader range of movements, including those in the frontal plane. The design is grounded in biomechanical principles and addresses the need for balanced natural movement during walking. The exoskeleton design enables a wide spectrum of movements and is not limited to a purely sagittal plane rotation.

The moment in each joint and the angular velocity were calculated to determine the motor property. At the ankle joint, the force from the ground reacts to the foot (GRF), and the weight of the foot creates torque while the subject walks. The force that occurs at the ankle joint can be explained by

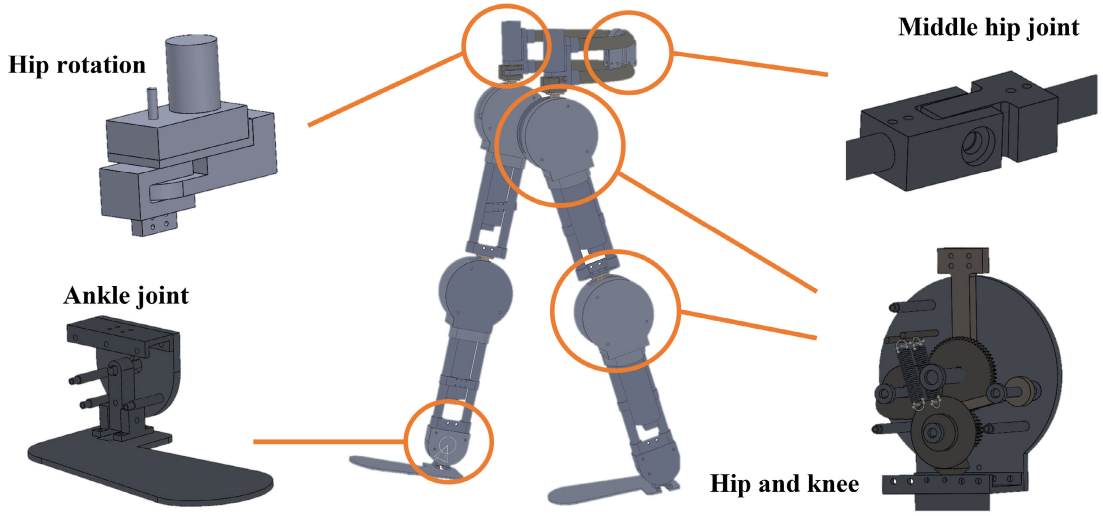

FIGURE 8. Overview of the proposed Robotic Exoskeleton with integration of the various components.

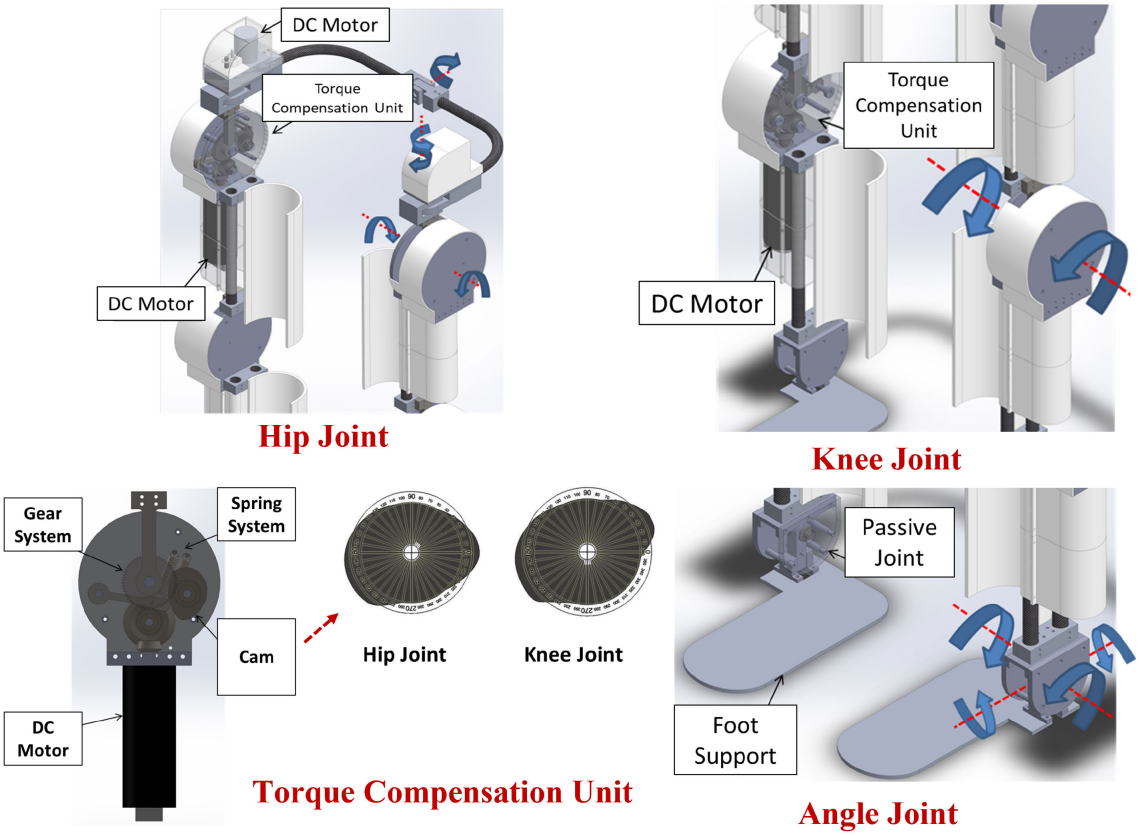

FIGURE 9. Overview of the Proposed Robotic Exoskeleton: External Structure and Joint Motions.

Newton's second law of motion $\Sigma F = ma$ in equations (13) and (14) [35], [36].

$$F_{ankle} + m_{foot}g - GRF = m_{foot}a_{y,foot} \tag{13}$$

$$F_{ankle} = m_{foot}g + GRF - m_{foot}a_{y,foot} \tag{14}$$

where F_{ankle} is a force that occurs at the ankle; m_{foot} is the weight of the foot; $a_{y,foot}$ is the acceleration in the y-axis of the foot; GRF is ground reaction force; g is the acceleration of gravity; Then the inertia of foot can be calculated by (15)

$$I_{foot} = m_{foot}r_{cog,foot}^2 \tag{15}$$

where I_{foot} is the moment of inertia of foot; $r_{cog,foot}$ is the length from toe to center of gravity of foot. The knee and hip joints are similar. The forces that affect the joint are from the previous joint reaction and the weight of each section. The

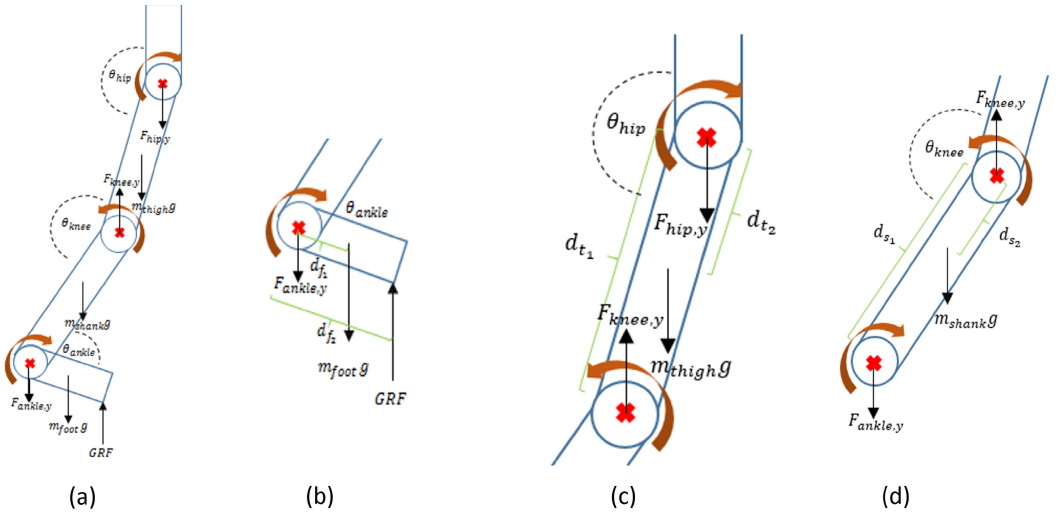

FIGURE 10. (a) Free body diagram of BART LAB EXO II, (b) Free body diagram of Foot section, (c) Free body diagram of Shank section (d) Free body diagram of Thigh section.

moment that appears at the joint is not only from these forces but it also contains the moment from the previous joint. The equation of knee and hip are shown in (16) to (17).

$$-F_{knee} + m_{shank}g + F_{ankle} = m_{shank}a_{y,shank} \tag{16}$$

By rearranging Equation 16, it can be expressed as:

$$F_{shank} = -m_{shank}a_{y,shank} + m_{shank}g + F_{ankle} \tag{17}$$

Then the inertia,

$$I = m_{shank}r^2_{cog,shank} \tag{18}$$

The equation of thigh and hip are shown in (19) to (20).

$$F_{hip} + m_{thigh}g - F_{knee}m_{thigh}a_{y,thigh} \tag{19}$$

$$F_{hip} = m_{thigh}a_{y,thigh} - m_{thigh}g - F_{knee} \tag{20}$$

In the coronal plane, the angular displacement is denoted by a positive sign (plus) in the clockwise direction and a negative sign (minus) in the counterclockwise direction illustrated in Fig. 11. Specifically, the analysis focuses on the hip's behavior within the context of the condition (26 degrees to 0 degrees) during the gait cycle, spanning from initial contact to pre-swing. This phase is addressed by (21), which can be expressed as

$$\begin{aligned}\sum \tau &= 0 \\ &= [\tau_{\text{Hip}}] - [Mg_{\text{total leg}} \cdot D_{\text{CoM(total leg)}} \cdot \cos(\theta_{\text{Hip (Ab)}})] \\ &\quad + [Ry \cdot D_{\text{total leg}} \cdot \cos(\theta_{\text{Hip (Ab)}}]\end{aligned} \tag{21}$$

D. ENERGY STORAGE SYSTEM

The ankle comprises four passive joints that facilitate specific movements essential for human locomotion [37], [38]. Dorsiflexion involves pulling the foot upward towards the shin and decreasing the angle between the foot and leg. This motion is utilized during the initial phase of the walking

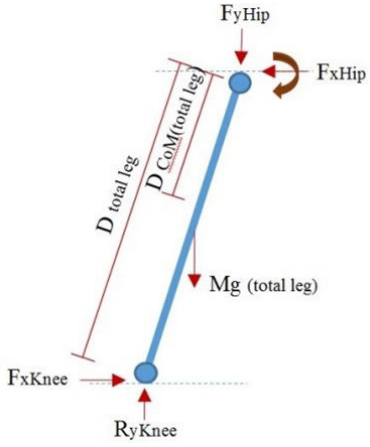

FIGURE 11. Hip in the coronal plane.

cycle when the foot lifts off the ground and the leg swings forward. In contrast, plantar flexion entails pushing the foot downwards, increasing the angle between the foot and the leg. This movement plays a vital role in propelling the body forward during the later phase of the walking cycle, when the foot pushes off the ground [39], [40], [41].

Additionally, inversion is the movement of tilting the sole of the foot inward toward the midline of the body, which is crucial for maintaining stability during weight-bearing activities, such as standing and walking on uneven surfaces. Conversely, eversion involves tilting the sole of the foot outward away from the midline to help maintain balance during weight-bearing activities [39].

Within the context of the aforementioned exoskeleton design, emphasis was placed on dorsiflexion and plantar flexion movements. The passive joint employs a spring-based design optimized to resist the torque resulting from body weight during dorsiflexion, thereby providing the necessary foot support and alignment during walking. Furthermore, the lowest joint attached allows for inversion and eversion

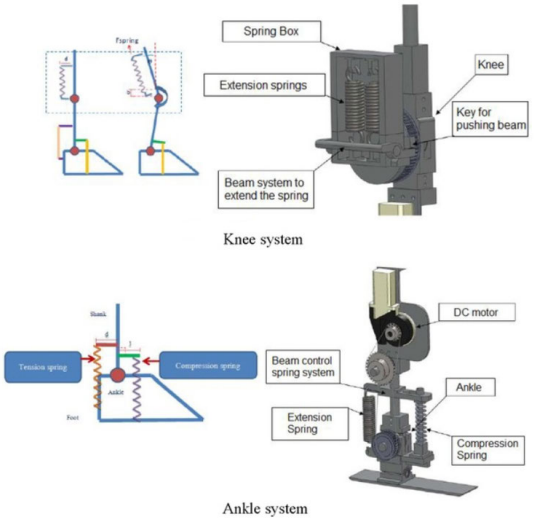

FIGURE 12. Mechanism of the spring-mechanical system in the knee and ankle joints.

movements, facilitated by torsion springs integrated between the flexion joint links and insole. The mechanism of the spring-mechanical system in the knee and ankle joints is illustrated in Fig. 12.

Fig. 13-a demonstrates the integration of the cam system with the spring system. The cam periodically activates the follower, making contact with its surface. The follower, attached to a spring fixed to the shaft, traces the cam's width at various angles according to the leg motion.

These passive joint configurations, which enable dorsiflexion, plantar flexion, inversion, and eversion, contribute to the efficient functioning of the ankle and enhance the overall lightweight and effective design of the exoskeleton. By replicating the natural gait patterns, the exoskeleton optimally assists wearers in maintaining proper foot positioning and achieving efficient propulsion during walking, thereby supporting their lower limb mobility.

The follower periodically moves up and down depending on the cam, and the cam depends on the angle of the leg attached to the same shaft of the cam. The follower tied to the spring brings up the spring and the spring is extended. Energy is stored in the spring, and during the high-torque requirement period, the cam is designed to have a decreasing slope. During this period, the force in spring takes the follower down and pushes the cam. Thus, the cam attached to the leg rotates more easily. The torque generated was reduced by the force of the spring that pulls itself back as shown in Fig. 13-b.

To calculate the torque reduced by the spring, the following equation is used:

$$\tau_{reduced} = \tau_{motion} - \tau_{spring} \tag{22}$$

where $\tau_{reduced}$ is the reduced output torque after compensation with the spring system. τ_{motion} is the general torque that occurs in each joint during the gait cycle.

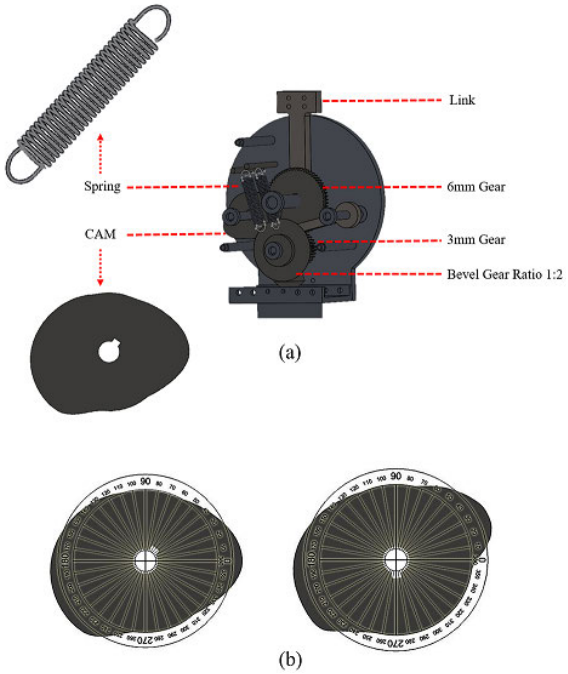

FIGURE 13. (a) CAM system integrated with spring and gear, (b) CAM used in the hip joint (left), knee joint (right) with degree label of increasing and decreasing period.

τ_{spring} is the torque produced by the spring when it is extended, calculated in Equation 23.

$$\tau_{spring} = F_{spring} \times r \tag{23}$$

$$F_{spring} = k \times x \tag{24}$$

In Equation 24, F_{spring} is the force of the spring when it is extended, where r is the reduction radius of the gear system. k is the spring constant. x is the length the spring is extended from its normal position.

E. SIGNAL ACTIVATOR AND ROBOT CONTROL SYSTEM

The control method for the lower-limb exoskeleton with the user's motion intention is crucial. Electroencephalography (EEG) and electrooculogram (EOG) signals are considered the most suitable signals for identifying the human intention of motion owing to their unique advantages [42]. EEG signals directly measure brain activity and offer insights into the neural processes linked to intentions and actions [43]. In contrast, EOG signals effectively detect eye movement patterns, thus complementing the intention recognition process [44], [45]. Combining EEG and EOG signals allows for a comprehensive interpretation of the neural and ocular dynamics related to human intention, leading to enhanced accuracy and reliability in intention recognition tasks.

The electrical properties of the brain always change when a person performs any activity [46]. The source of the EOG signal is the cornea-retinal potential (CRP), which is generated due to the movement of the eyeballs within the conductive environment of the skull [47]. Brain-computer interfaces (BCI) can classify EEG and EOG signals and

translate brain activities into useful commands for external devices [48], [49]. The system was activated by collecting thresholds in the beta-wave field and two types of EOG signals. To find the threshold, the subject will generate the signal by thinking, gazing down, gazing left, and gazing right for 2 seconds. The threshold was set at 70% of each maximum signal value. The command was executed when the signal value is higher than the threshold value. The architecture of the control system is shown in Fig. 14-a.

An eye signal is generated when the eyes begin moving. Gaze up-down and left-right represent the opposite directions of the signal. According to the 10-20 system, for EEG signals, the positive and negative electrodes are placed at the Fp2 and A2 positions, respectively. The ground electrode is placed in the other ear. The beta wave is detected by summing the range of 13-30 Hz for a second. The EOG signal was measured in two positions: vertical and horizontal lines. Four electrodes were placed on the sides of the left and right eyes and above and below the eye. The ground electrode was the same electrode for EEG measurement. To determine left gazing and right gazing or looking downward, the amplitude is summed for a larger value. To activate the robot, the user's brain signal (EEG) and eye movement signal (EOG) is fused with the robot control system to comprehend human intention and predict movement, as shown in Fig. 14-b. The PID feedforward-based motion control technique was used to enhance system dynamics and stability.

The digital filter was applied in the range of the beta waveform 13-30 Hz in each trigger, which was 100 samples per trigger. The third-order Butterworth band-pass filter was chosen because of its low rippling. A higher order produces a clear signal, but it delays it more. Equation (25) represents the filter transfer function:

$$| H(j\omega) |^2 = \frac{G}{1 + (\frac{\omega}{\omega_c})^{2n}} \tag{25}$$

where G is the DC gain at zero frequency, n is the order of the filter and $\omega_c$is the cutoff frequency. In order to determine the transfer function $H(s)$, because of the property of Laplace transform when,

$$| H(j\omega) |^2 = H(s)H(-s) \tag{26}$$

then $s = j\omega$

$$H(s)H(-s) = \frac{G^2}{1 + (\frac{-s^2}{\omega_c^2})^n} \tag{27}$$

The n-pole of this transfer function (27) is represented by a circle of radius in the negative real half-plane of s. The m-th pole is posed by (28) and (29).

$$\frac{-s_k^2}{\omega_c^2} = e^{\frac{j(2m-1)\pi}{n}} \tag{28}$$

where m = 1, 2, 3…n Hence;

$$s_k = e^{\frac{j(2m-1)\pi}{2n}} \tag{29}$$

Fig. 15 shows the raw signal of the EEG waveform, before and after applying the filter

After filtering, the post-filter signal is converted from the time domain to the frequency domain using Discrete Fourier Transform (DTFT) equations (30) and (31) as follows:

$$X(f_m) = \sum_{n=0}^{N-1} x(n) e^{-2j\pi n f_m} T_s \tag{30}$$

$$f_m = \frac{m f_s}{n} \tag{31}$$

where N denotes the number of points in the waveform, m denotes the family of members and f_s denotes the sampling frequency. The power of the amplitude in the frequency domain is called the power spectrum density and is detected as (32).

$$w(n) = 0.54 - 0.46 \cos(\frac{2\pi n}{N-1}) \tag{32}$$

The beta wave was detected by summing the range of 13-30 Hz per second. An example of an EEG signal after the transfer is shown in Fig.15.

EOG signals were measured along two vertical and horizontal lines. Four electrodes were placed on the left and right sides as well as above and underneath the eyes. The EOG signal was collected using an EOG circuit, as shown in Fig. 16. This circuit consists of 10000 times amplified: high-pass filter (0.1 Hz), low-pass filter (10 Hz), and Twin-T notch filter (50 Hz). After the analog processes, the signal was converted to a digital signal using NI USB-6008 (National Instruments Corp. Austin, Texas, USA) and sent to MATLAB R2020b (The MathWorks, Inc., Massachusetts, United States) with the same sampling rate and sample per trigger of the EEG signal. A third-order Butterworth bandpass filter is added in the range of 0.1-10 Hz by using the same equation as the EEG filter. This was used to determine the left gazing and right gazing or looking downward, and the amplitude was summed to obtain a larger value within 2 seconds, the results are presented in Fig. 17.

To achieve precise control of the exoskeleton, a proportional-integral-derivative (PID) control algorithm was implemented. This algorithm plays a crucial role in enhancing the accuracy and stability of the system by continuously monitoring the position of the exoskeleton and adjusting the control signals accordingly, thereby ensuring precise and responsive movements.

For motor control and encoder data reception, an ET-Base dsPIC30F4011 (Microchip Technology Inc. Arizona, USA) microcontroller was employed. This microcontroller provides a reliable and efficient platform for controlling the motors driving the movements of the exoskeleton. In addition, it facilitates the reception and processing of data from the encoders, which provides crucial feedback regarding the exoskeleton's joint positions. MATLAB was utilized as the interface to facilitate the interaction between the control system and the exoskeleton.

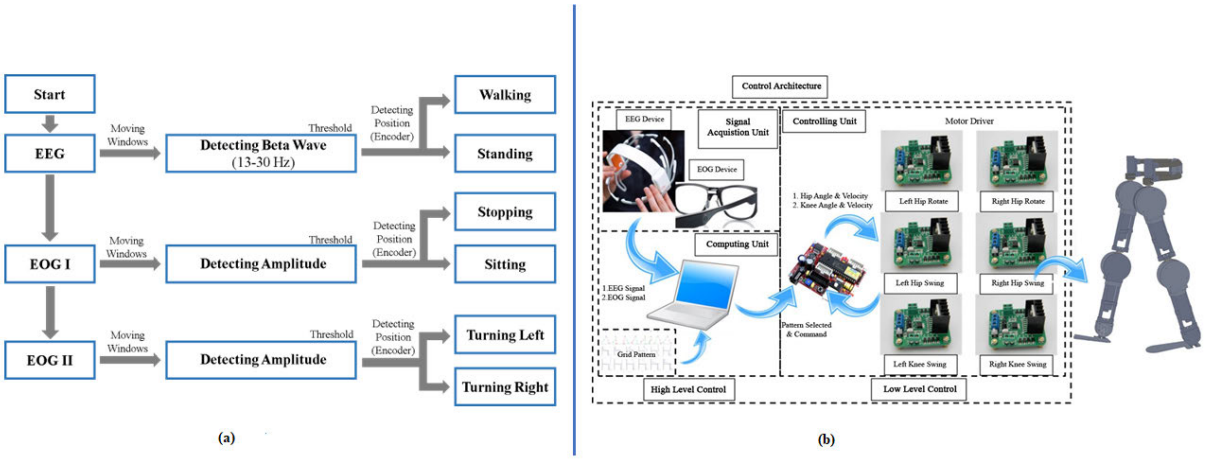

FIGURE 14. (a) Signal activator control system architecture, (b) Robot control system architecture.

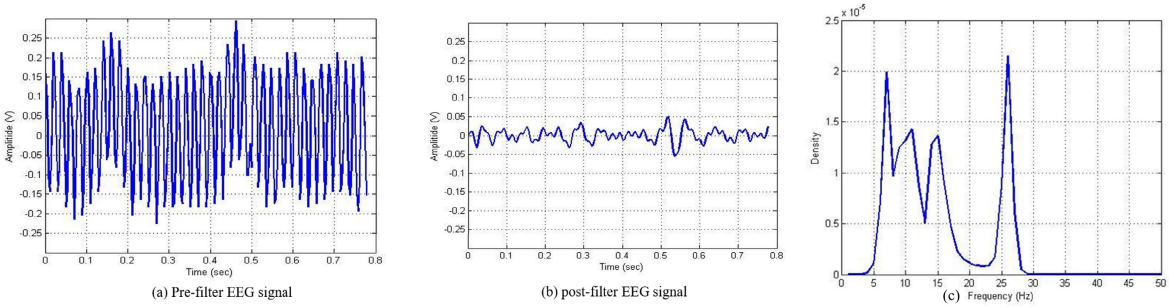

FIGURE 15. (a) Pre-filter EEG signal, (b) post-filter of EEG signal, and (c)Filter EEG in frequency domain.

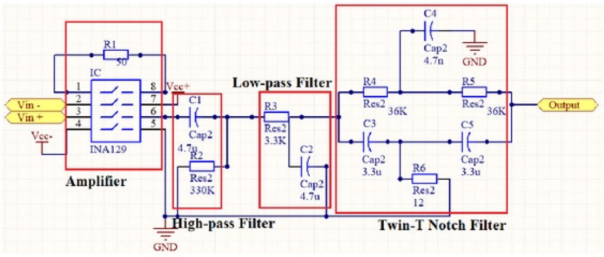

FIGURE 16. EOG circuit.

In the course of this research, computational tasks and simulations were executed on a workstation with the following specifications: the central processing unit (CPU) was an Intel(R) Core(TM) i5-7600 operating at a clock speed of 3.50 GHz. The system boasted a memory capacity of 8.00 GB, and the installed operating system was a 64-bit platform with an x64-based processor. This computing environment provided the necessary computational resources to perform complex numerical analyses and simulations, ensuring the accuracy and precision of the results reported in this study.

The working flow of the system is shown in Fig. 18, which provides a visual representation of the sequential operations involved in the control process. This flowchart outlines the step-by-step execution of tasks, including signal detection, processing, and motor control, ensuring well-coordinated and synchronized operation of the exoskeleton.

IV. RESULTS AND DISCUSSION

The following section provides a comprehensive account of the specific actions undertaken, encompassing the GRF estimation, motion analysis, and structural analysis of our exoskeleton. These endeavors played a critical role in evaluating the performance and effectiveness of our proposed approach, ensuring result accuracy, and validating the feasibility of our design.

A. ESTIMATION OF GROUND REACTION FORCE

To calculate the GRF at the foot joint during sit-to-stand and stand-to-sit motions as mentioned in Section III. We used MATLAB simulation, which incorporates constants, parameters, and equations to determine the torques at the hip, knee, and ankle joints based on body weight, leg segment masses, lengths, and angles. For this, we considered a male person with a body weight of 70 kg and a height of 175 cm. Reaction forces at the foot joint were computed by dividing the knee torque by the length of the foot segment. Additionally, the coordinates of the foot joint were calculated for both sitting and standing positions. The plots provide insights into the direction and magnitude of the GRF, aiding the understanding of the force distribution

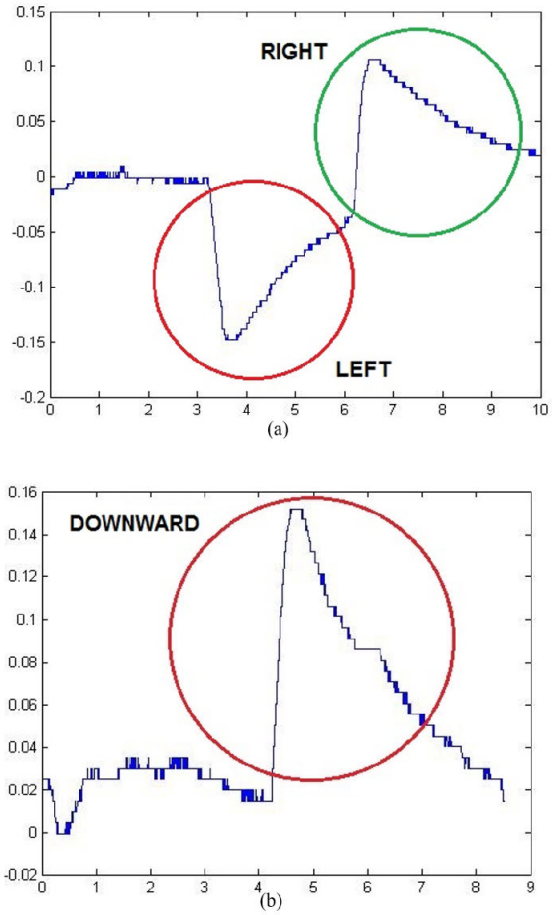

FIGURE 17. (a) Post filter EOG signal (left-right) (b) Post filter EOG signal (down).

and variation throughout the motions. These findings are crucial for the design and analysis of assistive devices such as exoskeletons. The simulation determines the coordinates of the foot joint and visualizes the reaction forces in a $3D$ plot (Fig. 19). Although the simulation itself is not directly related to the proposed exoskeleton, it serves as a crucial preliminary study that underpins the foundation of our research. By gaining insight into the direction and magnitude of the GRF, we can better understand the force distribution and variations throughout these motions. The knowledge derived from this simulation is instrumental in informing the design and analysis of assistive devices, such as exoskeletons, ensuring that they are optimized to support and enhance the user's lower limb movements.

The reaction forces at the foot joint during the sit-to-stand and stand-to-sit motions are shown in the generated graphs (Fig. 19). In the sit-to-stand graph, represented by red arrows, the x, y, and z coordinates of the foot joint were used to visualize the forces. Similarly, the stand-to-sit graph, represented by blue arrows, shows the reaction forces during the respective motions. These visualizations provided valuable insights into the load distribution and

TABLE 1. Angle limitation table.

Joints	Angle (Degree)	Joint Type
Middle Hip Joint	-20 to 20	Passive
Hip Rotation Joint	-30 to 30	Active
Hip Sagittal Joint	-20 to 90	Active
Knee Joint	0 to 90	Active
Ankle Sagittal Joint	0 to 20	Passive
Ankle Inversion/Eversion	-10 to 10	Passive

balance requirements of the lower limbs during sit-to-stand and stand-to-sit movements.

B. ENERGY STORAGE SYSTEM

After calculating the reduced torque from the spring, it was determined that the spring constant of 14 N/m provided the best results. Lower spring constants result in a lower torque. For the exoskeleton robot, motors with high torque (9 Nm) are used in the hip and knee joints because they can provide sufficient torque after reduction by the spring system and gear ratio. A 5 Nm motor was utilized for the rotation joints of the hip. Two springs with a constant of 7 N/m were used to achieve the highest torque efficiency in the spring system, as determined by calculations. The torque on the joints was significantly reduced after the implementation of the spring cam system, as illustrated in Fig. 20.

C. MOTION ANALYSIS

When the knee joint absorbs body weight, the highest torque develops on the knee, and the other peak occurs when the leg attempts to push off. At the hip, all peaks appeared when it acted at the maximum angle. Fig. 21 shows the torque that occurs in one cycle of walking. Sit-to-stand and stand-to-sit are reversible. In addition, the torque characteristic and the mirror value of the torque are generated, as shown in Fig. 22-23. The maximum value occurred when the hip and knee joints increased their angles. The maximum moment that occurs in each joint for turning is shown in Fig. 24-25. This is one step of turning at 30 degrees. The angle of each joint is defined in terms of the relative angle. In the turning motion, the angle changed slightly for each joint. One cycle of turning consisted of three steps for 90 degrees turns. Each graph represents the turning step. The changes in the hip and knee of the outer leg were similar. In addition, the inner leg, hip angle, and a knee changed in the same direction. For the rotation hip, both the inner and outer legs slowly rotated to 30 degrees in each step. The range of the angle in each joint and each motion can be concluded from Table -1.

To determine the speed of the motor for the driving unit, angular velocity is required. Angle and angular velocity were used as databases for controlling the motors. Then, the set of speeds for each motion was evaluated. Table - 2 shows the speed in RPM that occurs in each joint and motion.

D. STRUCTURAL ANALYSIS

The analysis was performed in both the hip and knee joints during the walking, sit-to-stand, and stand-to-sit positions.

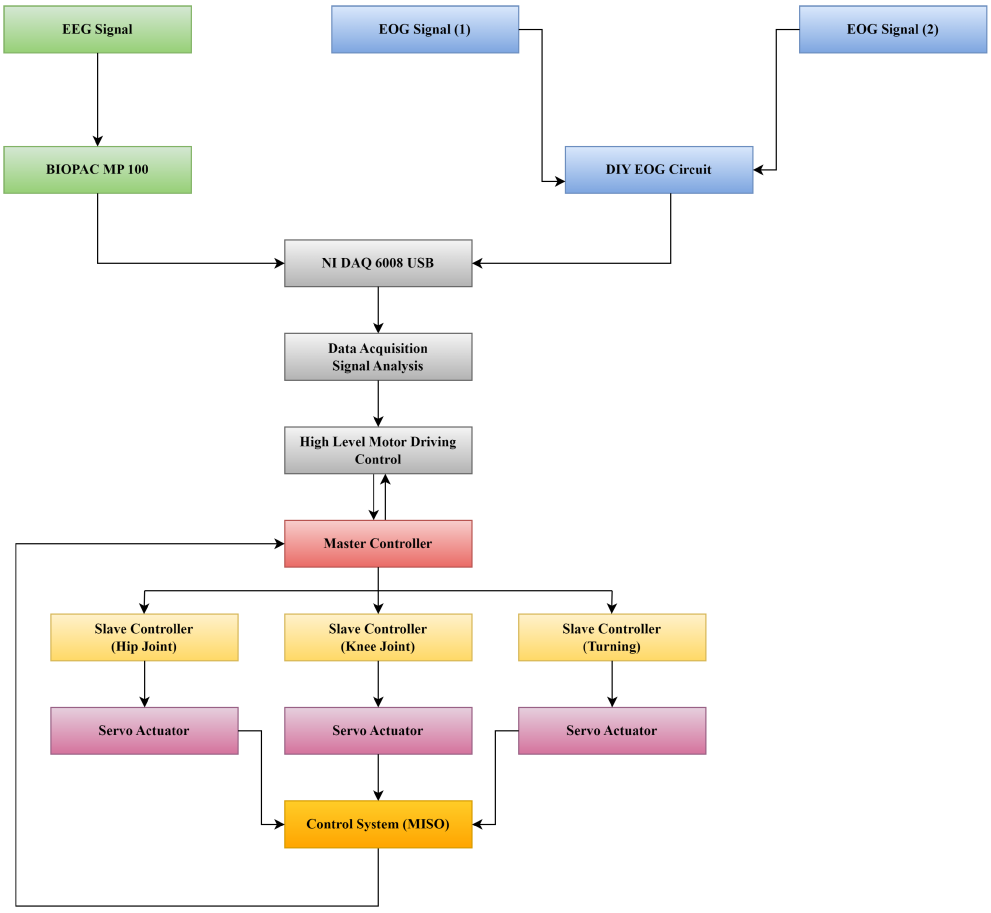

FIGURE 18. The flowchart of the workflow.

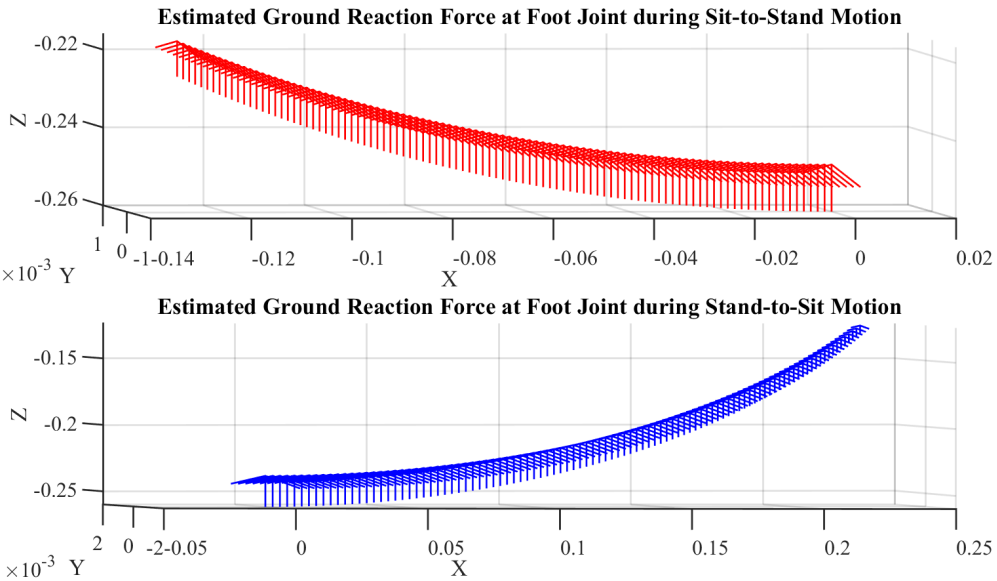

FIGURE 19. The Estimated Ground Reaction Force (GRF) was estimated using MATLAB simulations for sit-to-stand and stand-to-sit motions. In the top subplot, the red quiver plot illustrates the GRF at the foot joint during sit-to-stand motion. The bottom subplot displays the blue quiver plot showing the GRF at the foot joint during the stand-to-sit motion. The arrows represent the direction and magnitude of the GRF.

The results of the experiment applying the spring system equation to the maximum moment that occurs in each joint are shown below. Incorporating equations 22, 23, and 24 into a MATLAB program allowed for the calculation of the

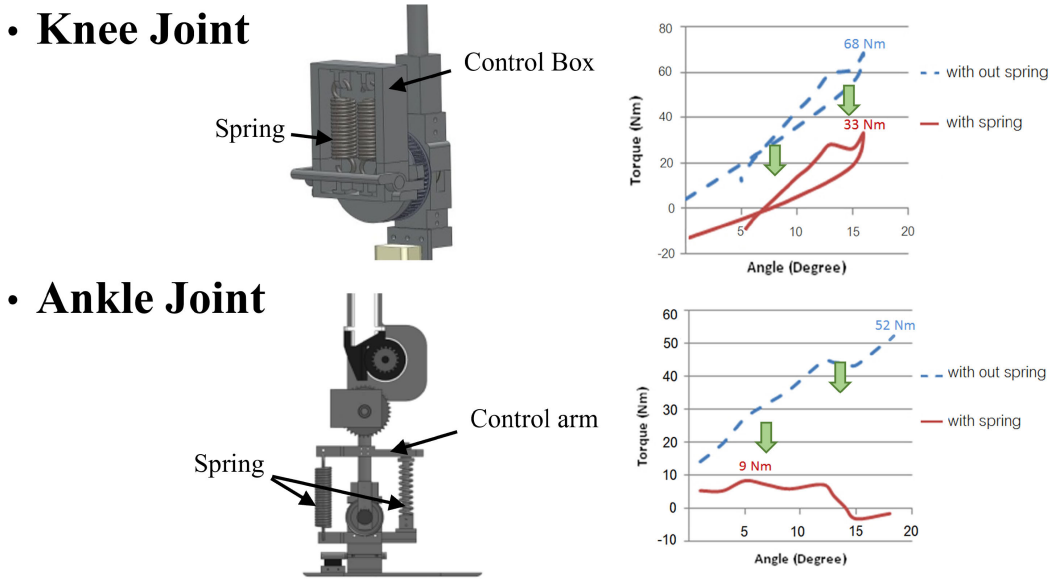

FIGURE 20. Before and After: The implementation of the spring cam system drastically reduced the torque on the joints, as seen in the figure.

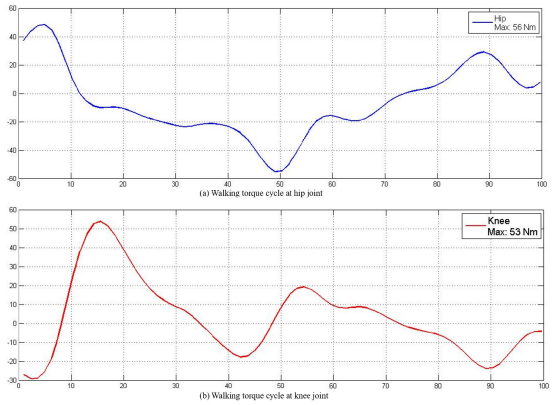

FIGURE 21. Walking torque cycle (a) hip joint (b) knee joint.

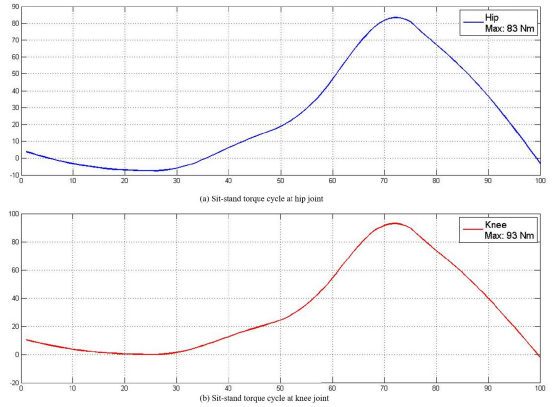

FIGURE 22. Sit-stand torque cycle (a) hip joint (b) knee joint.

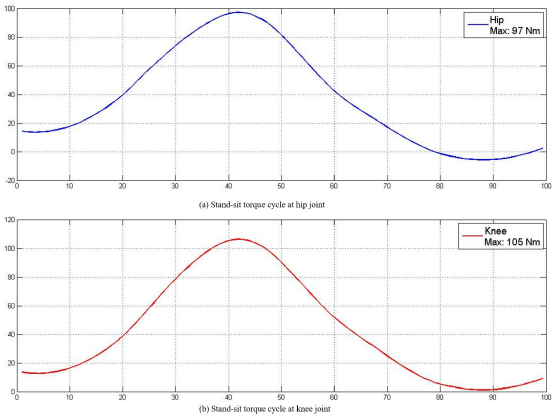

FIGURE 23. Stand-sit torque cycle (a) hip joint (b) knee joint.

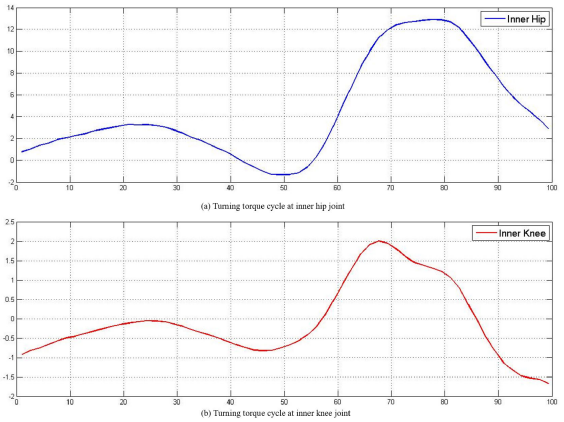

FIGURE 24. Turning torque cycle (a) inner hip joint (b) inner knee joint.

reduced torque from the spring, with a spring constant of 14 Nm yielding the optimal outcome. Using a lower spring constant would result in a smaller reduction in torque, while a higher spring constant would hinder the robot's ability

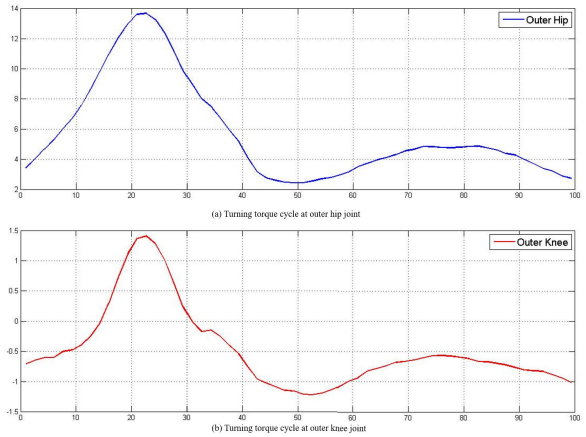

FIGURE 25. Turning torque cycle (a) outer hip joint (b) outer knee joint.

TABLE 2. Torque and speed in each motion.

Motion	Maximum Torque (Nm)		Maximum Speed (RPM)	
	Hip	Knee	Hip	Knee
Walking	56	53	10	13.9
Sit-Stand w/ Arm Support	97	105	8.8	11.2
Sit-Stand w/o Arm Support	83	93	10.2	9.1
Turning	14	2	5.5	4.6

to overcome the spring force. The torque reduction was observed to be approximately $34 - 36$ Nm in each joint. The hip torque is reduced and controlled during walking by adding spring and cam mechanisms, as shown in Fig. 26 (a). The knee torque is reduced and controlled by applying the spring and cam mechanism throughout the walking cycle when compared to the system without the spring and cam mechanisms, as shown in Fig. 26 (b). The values obtained were more desirable than those of the previous version of the BART LAB EXO-I [7]. The hip torque was reduced compared to the previous version during the sit-to-stand and stand-to-sit phases. The movement was controlled by applying spring and cam mechanisms throughout the cycle, as shown in Fig. 26 (c). The knee torque is also comparatively reduced during the sit-to-stand and stand-to-sit phases when compared to the system without the spring and cam mechanism, as shown in Fig. 26 (d).

In conclusion, the focus of our work was on the development of a lower-limb exoskeleton intended to assist and rehabilitate those who have lost mobility as a result of SCI. We added a new spring and camshaft system to the exoskeleton structure to address the problems associated with energy storage present in prior designs. By efficiently absorbing the user's body weight as potential energy in the springs, which was then released through the cam design, this novel solution allowed us to lower energy requirements. We investigated the performance of the exoskeleton in terms of ground response forces, mechanical design, and activation using a BCI-based signal activator through a series of motion experiments and data analysis. The results of our study demonstrate the effectiveness of our exoskeleton design in providing support

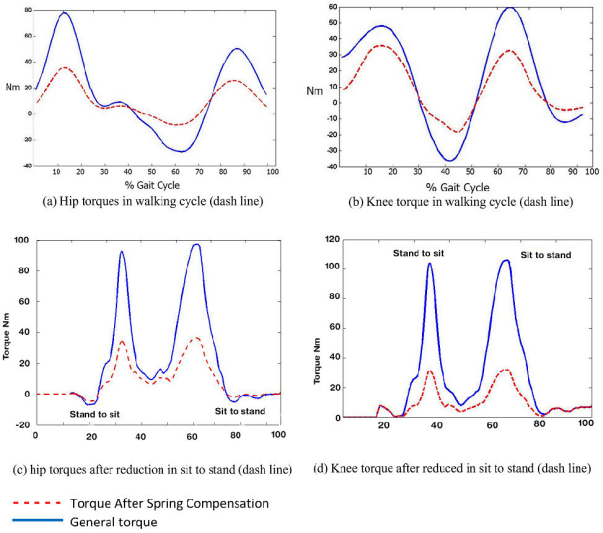

FIGURE 26. Torques in the walking cycle (a) Hip torques in the walking cycle (dash line) (b) Knee torque in the walking cycle (dash line). Torques after reduction in sit-to-stand motion (c) hip torques after reduction in sit-to-stand (dash line) (d) Knee torque after reduction in sit-to-stand (dash line.

and rehabilitation for physically challenged individuals with SCI. The spring and camshaft systems were effectively integrated to reduce energy consumption while still providing sufficient support to the user. The results of this study pave the way for further exoskeleton technology development, which will improve mobility and rehabilitation options for patients with spinal cord injuries.

V. CONCLUSION

A low-cost lower-limb exoskeleton with a custom-made energy-storage system was designed, fabricated, and tested. By developing the springs and camshafts method of energy restoration, the motor load is reduced, and the torque compensation is improved when compared to the previous version, BART LAB EXO I. The exoskeleton provides minimum torque assist at the hip and knee joints, which allows the wearer to apply a comparatively low torque at these joints and prevent strain. The BART LAB EXO II model functions on a predefined cycle of the walking gait. The results obtained are desirable when considering the limitations of microcontroller functionality. In our future work, we will design a lower limb exoskeleton that is compactable and customizable for every individual affected with paraplegia. Machine-learning approaches were incorporated to improve the compatibility of the proposed exoskeleton.

ACKNOWLEDGMENT

The authors express their gratitude to the individuals who contributed significantly to this study, including the members of the Center for Biomedical and Robotics Technology (BART LAB), namely A. Temram, W. Banchadit, T. Sukwan, W. Sirisopha, and N. Intawachirarat, for their involvement and invaluable support. They would also like to thank

Choladawan Moonjaita, Nantida Nillahoot, and Yuttana Itsarachaiyot for their expertise and assistance, which played a crucial role in the successful completion of the research.

REFERENCES

[1] M. Kashif, S. Jones, H. I. Haider Darain, A. Raqib, and A. A. Butt, "Factors influencing the community integration of patients following traumatic spinal cord injury: A systematic review," *J. Pakistan Med. Assoc.*, vol. 69, no. 1336, pp. 1337–1343, 2019.

[2] D. Calafiore, F. Negrini, N. Tottoli, F. Ferraro, O. Ozyemisci-Taskiran, and A. de Sire, "Efficacy of robotic exoskeleton for gait rehabilitation in patients with subacute stroke : A systematic review," *Eur. J. Phys. Rehabil. Med.*, vol. 58, no. 1, p. 1, Mar. 2022.

[3] S. Qiu, Z. Pei, C. Wang, and Z. Tang, "Systematic review on wearable lower extremity robotic exoskeletons for assisted locomotion," *J. Bionic Eng.*, vol. 20, no. 2, pp. 436–469, Mar. 2023.

[4] A. Kapsalyamov, P. K. Jamwal, S. Hussain, and M. H. Ghayesh, "State of the art lower limb robotic exoskeletons for elderly assistance," *IEEE Access*, vol. 7, pp. 95075–95086, 2019.

[5] F. Gao, Y. Liu, and W.-H. Liao, "Cam profile generation for cam-spring mechanism with desired torque," *J. Mech. Robot.*, vol. 10, no. 4, pp. 1–2, Aug. 2018.

[6] J. S. Schroeder and J. C. Perry, "Development of a series wrapping cam and energy-storing spring system for application in wearable robotic arm supports," *Technol. Innov.*, vol. 20, nos. 1–2, pp. 21–36, Nov. 2018.

[7] W. Banchadit, A. Temram, T. Sukwan, P. Owatchaiyapong, and J. Suthakorn, "Design and implementation of a new motorized-mechanical exoskeleton based on CGA patternized control," in *Proc. IEEE Int. Conf. Robot. Biomimetics (ROBIO)*, Dec. 2012, pp. 1668–1673.

[8] D. A. Winter, *Biomechanics and Motor Control of Human Movement*. Hoboken, NJ, USA: Wiley, 2009.

[9] J. K. Moore, S. K. Hnat, and A. J. van den Bogert, "An elaborate data set on human gait and the effect of mechanical perturbations," *PeerJ*, vol. 3, p. e918, Apr. 2015.

[10] T. Xue, Z. Wang, T. Zhang, M. Zhang, and Z. Li, "The control system for flexible hip assistive exoskeleton," in *Proc. IEEE Int. Conf. Robot. Biomimetics (ROBIO)*, Dec. 2018, pp. 697–702.

[11] T. Zhang, M. Tran, and H. H. Huang, "NREL-exo: A 4-DoFs wearable hip exoskeleton for walking and balance assistance in locomotion," in *Proc. IEEE/RSJ Int. Conf. Intell. Robots Syst. (IROS)*, Sep. 2017, pp. 508–513.

[12] T. Lee, D. Lee, B. Song, and Y. S. Baek, "Design and control of a polycentric knee exoskeleton using an electro-hydraulic actuator," *Sensors*, vol. 20, no. 1, p. 211, Dec. 2019.

[13] K. I. K. Sherwani, N. Kumar, A. Chemori, M. Khan, and S. Mohammed, "RISE-based adaptive control for EICoSI exoskeleton to assist knee joint mobility," *Robot. Auto. Syst.*, vol. 124, Feb. 2020, Art. no. 103354.

[14] X. Wang, S. Guo, B. Qu, M. Song, and H. Qu, "Design of a passive gait-based ankle-foot exoskeleton with self-adaptive capability," *Chin. J. Mech. Eng.*, vol. 33, no. 1, pp. 1–11, Dec. 2020.

[15] P. G. Vinoj, S. Jacob, V. G. Menon, S. Rajesh, and M. R. Khosravi, "Brain-controlled adaptive lower limb exoskeleton for rehabilitation of post-stroke paralyzed," *IEEE Access*, vol. 7, pp. 132628–132648, 2019.

[16] C. Jarrett and A. J. McDaid, "Robust control of a cable-driven soft exoskeleton joint for intrinsic human–robot interaction," *IEEE Trans. Neural Syst. Rehabil. Eng.*, vol. 25, no. 7, pp. 976–986, Jul. 2017.

[17] X. Wan, Y. Liu, Y. Akiyama, and Y. Yamada, "Monitoring contact behavior during assisted walking with a lower limb exoskeleton," *IEEE Trans. Neural Syst. Rehabil. Eng.*, vol. 28, no. 4, pp. 869–877, Apr. 2020.

[18] A. J. Young and D. P. Ferris, "State of the art and future directions for lower limb robotic exoskeletons," *IEEE Trans. Neural Syst. Rehabil. Eng.*, vol. 25, no. 2, pp. 171–182, Feb. 2017.

[19] A. Plaza, M. Hernandez, G. Puyuelo, E. Garces, and E. Garcia, "Lower-limb medical and rehabilitation exoskeletons: A review of the current designs," *IEEE Rev. Biomed. Eng.*, vol. 16, pp. 278–291, 2023.

[20] R. L. Hybart and D. P. Ferris, "Embodiment for robotic lower-limb exoskeletons: A narrative review," *IEEE Trans. Neural Syst. Rehabil. Eng.*, vol. 31, pp. 657–668, 2023.

[21] G. Aguirre-Ollinger, J. E. Colgate, M. A. Peshkin, and A. Goswami, "Inertia compensation control of a one-degree-of-freedom exoskeleton for lower-limb assistance: Initial experiments," *IEEE Trans. Neural Syst. Rehabil. Eng.*, vol. 20, no. 1, pp. 68–77, Jan. 2012.

[22] L. Xie, G. Huang, L. Huang, S. Cai, and X. Li, "An unpowered flexible lower limb exoskeleton: Walking assisting and energy harvesting," *IEEE/ASME Trans. Mechatronics*, vol. 24, no. 5, pp. 2236–2247, Oct. 2019.

[23] G. Nagymáté and R. M. Kiss, "Application of optitrack motion capture systems in human movement analysis a systematic literature review," *Recent Innov. Mechatronics*, vol. 5, no. 1, pp. 1–9, 2018.

[24] M. Cardona et al., "Gait capture systems," in *Exoskeleton Robots for Rehabilitation and Healthcare Devices*. Singapore: Springer, 2020, pp. 27–42.

[25] C. L. Vaughan, B. L. Davis, and J. C. O'connor, *Dynamics of Human Gait*. Champaign, IL, USA: Human Kinetics Publishers, 1992.

[26] I. Roupa, M. R. da Silva, F. Marques, S. B. Gonçalves, P. Flores, and M. T. da Silva, "On the modeling of biomechanical systems for human movement analysis: A narrative review," *Arch. Comput. Methods Eng.*, vol. 29, no. 7, pp. 4915–4958, Nov. 2022.

[27] D. B. Fineberg, P. Asselin, N. Y. Harel, I. Agranova-Breyter, S. D. Kornfeld, W. A. Bauman, and A. M. Spungen, "Vertical ground reaction force-based analysis of powered exoskeleton-assisted walking in persons with motor-complete paraplegia," *J. Spinal Cord Med.*, vol. 36, no. 4, pp. 313–321, Jul. 2013.

[28] T. Hsiao, K. Yip, and Y.-J. Chiu, "Estimation of ground reaction forces based on knee joint acceleration of lower-limb exoskeletons," in *Proc. Int. Autom. Control Conf. (CACS)*, Nov. 2020, pp. 1–6.

[29] G. Serrancolí, A. Falisse, C. Dembia, J. Vantilt, K. Tanghe, D. Lefeber, I. Jonkers, J. De Schutter, and F. De Groote, "Subject-exoskeleton contact model calibration leads to accurate interaction force predictions," *IEEE Trans. Neural Syst. Rehabil. Eng.*, vol. 27, no. 8, pp. 1597–1605, Aug. 2019.

[30] S. Winiarski and A. Rutkowska-Kucharska, "Estimated ground reaction force in normal and pathological gait," *Acta Bioeng. Biomechanics*, vol. 11, no. 1, pp. 53–60, 2009.

[31] H. R. Yamasaki, H. Kambara, and Y. Koike, "Dynamic optimization of the sit-to-stand movement," *J. Appl. Biomechanics*, vol. 27, no. 4, pp. 306–313, Nov. 2011.

[32] M. Cardona, V. K. Solanki, and C. E. G. Cena, *Exoskeleton Robots for Rehabilitation and Healthcare Devices*. Cham, Switzerland: Springer, 2020.

[33] S. Xie, *Advanced Robotics for Medical Rehabilitation* (Springer Tracts in Advanced Robotics), vol. 108, no. 1. Cham, Switzerland: Springer, 2016, p. 357.

[34] R. Colombo and V. Sanguineti, *Rehabilitation Robotics: Technology and Application*. New York, NY, USA: Academic, 2018.

[35] A. V. C. Borisov and A. V. Chigarev, *Mathematical Models of Exosceleton: Dynamics, Strength, Control*, vol. 431. Berlin, Germany: Springer Nature, 2022.

[36] T. Tan, D. P. Chiasson, H. Hu, and P. B. Shull, "Influence of IMU position and orientation placement errors on ground reaction force estimation," *J. Biomechanics*, vol. 97, Dec. 2019, Art. no. 109416.

[37] T. Purevsuren, K. Kim, M. Batbaatar, S. Lee, and Y. H. Kim, "Influence of ankle joint plantarflexion and dorsiflexion on lateral ankle sprain: A computational study," *Proc. Inst. Mech. Eng., H, J. Eng. Med.*, vol. 232, no. 5, pp. 458–467, May 2018.

[38] L. Li, A. Gollhofer, H. Lohrer, N. Dorn-Lange, G. Bonsignore, and D. Gehring, "Function of ankle ligaments for subtalar and talocrural joint stability during an inversion movement—An in vitro study," *J. Foot Ankle Res.*, vol. 12, no. 1, pp. 1–8, Dec. 2019.

[39] H. Xia, J. Kwon, P. Pathak, J. Ahn, P. B. Shull, and Y.-L. Park, "Design of a multi-functional soft ankle exoskeleton for foot-drop prevention, propulsion assistance, and inversion/eversion stabilization," in *Proc. 8th IEEE RAS/EMBS Int. Conf. Biomed. Robot. Biomechatronics (BioRob)*, Nov. 2020, pp. 118–123.

[40] C. L. Brockett and G. J. Chapman, "Biomechanics of the ankle," *Orthopaedics Trauma*, vol. 30, no. 3, pp. 232–238, 2016.

[41] C. M. Thalman and H. Lee, "Design and validation of a soft robotic ankle-foot orthosis (SR-AFO) exosuit for inversion and eversion ankle support," in *Proc. IEEE Int. Conf. Robot. Autom. (ICRA)*, May 2020, pp. 1735–1741.

[42] W.-D. Chang, "Electrooculograms for human–computer interaction: A review," *Sensors*, vol. 19, no. 12, p. 2690, Jun. 2019.

[43] M. Wairagkar, Y. Hayashi, and S. J. Nasuto, "Exploration of neural correlates of movement intention based on characterisation of temporal dependencies in electroencephalography," *PLoS ONE*, vol. 13, no. 3, Mar. 2018, Art. no. e0193722.

[44] M. Zhao, H. Gao, W. Wang, and J. Qu, "Research on human-computer interaction intention recognition based on EEG and eye movement," *IEEE Access*, vol. 8, pp. 145824–145832, 2020.
[45] C.-T. Lin, W.-L. Jiang, S.-F. Chen, K.-C. Huang, and L.-D. Liao, "Design of a wearable eye-movement detection system based on electrooculography signals and its experimental validation," *Biosensors*, vol. 11, no. 9, p. 343, Sep. 2021.
[46] M. Bigliassi, C. I. Karageorghis, G. K. Hoy, and G. S. Layne, "The *way you make me feel*: Psychological and cerebral responses to music during real-life physical activity," *Psychol. Sport Exercise*, vol. 41, pp. 211–217, Mar. 2019.
[47] A. B. Usakli, S. Gurkan, F. Aloise, G. Vecchiato, and F. Babiloni, "On the use of electrooculogram for efficient human computer interfaces," *Comput. Intell. Neurosci.*, vol. 2010, Oct. 2010, Art. no. 135629.
[48] S. Paszkiel, *Analysis and Classification of EEG Signals for Brain-Computer Interfaces*. Cham, Switzerland: Springer, 2020.
[49] R. P. Rao, *Brain-Computer Interfacing: An Introduction*. Cambridge, U.K.: Cambridge Univ. Press, 2013.

BRANESH M. PILLAI (Member, IEEE) received the bachelor's degree from Anna University, Chennai, India, in 2007, the master's (by Research) degree in control systems from the University of Moratuwa, Moratuwa, Sri Lanka, in 2013, and the Ph.D. degree in biomedical engineering (medical robotics) from Mahidol University, Nakhon Pathom, Thailand, in 2019. He is currently a Faculty Member with the Center for Biomedical and Robotics Technology (BART LAB), Faculty of Engineering, Mahidol University. His research interests include medical robotics and the related to advanced motion control, robot-assisted surgery, biomechanics, and rough terrain rescue robots.

PEERAPAT OWATCHAIYAPONG received the bachelor's degree in mechanical engineering from Mahidol University and the master's degree in mechanical engineering from Chulalongkorn University, Thailand. He is currently a Lecturer with the Department of Mechanical Engineering, Faculty of Industrial Education, Rajamangala University of Technology, Phra Nakhon, Thailand. His research interests include mechanical design for medical robotics and navigation, advancing medical technology, and robotics.

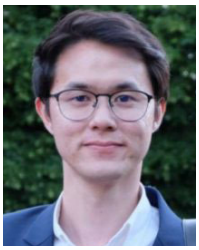

SHEN TRERATANAKULCHAI (Member, IEEE) received the B.Sc. and M.Sc. degrees in biomedical engineering from Mahidol University, Thailand, in 2012 and 2016, respectively, and the Ph.D. degree in mechanical engineering from Imperial College London, U.K., in 2022. He is currently a Lecturer with the Department of Biomedical Engineering, Mahidol University, where he conducts research with the Centre for Biomedical and Robotics Technology (BART LAB). His research interests include soft robotics and mechatronics for diagnostics, surgical instruments, surgical intervention, and human–machine interfaces.

DILEEP SIVARAMAN (Graduate Student Member, IEEE) received the integrated M.Sc. degree in physics from Amrita Vishwa Vidyapeetham University, India, in 2012. He is currently pursuing the Ph.D. degree in biomedical engineering (medical robotics) with the Center for Biomedical and Robotics Technology (BART LAB), Faculty of Engineering, Mahidol University, Thailand. His research interests include advanced motion control, sensor fusion, medical robotics, and rescue robotics along the direction of dynamics and control.

SONGPOL ONGWATTANAKUL (Member, IEEE) received the bachelor's degree in computer engineering from the King Mongkut's University of Technology Thonburi, Thailand, in 1994, the master's degree in computer science from The University of Edinburgh, U.K., in 1997, and the Ph.D. degree in electrical engineering from The University of Alabama, in 2003. He is currently the Executive Director of the Center for Biomedical and Robotics Technology (BART LAB), Mahidol University, and the Director of the Biomedical Cloud Computing Laboratory. His research interests include cloud computing in the healthcare industry and healthcare information systems big data in healthcare.

JACKRIT SUTHAKORN (Member, IEEE) received the bachelor's degree in mechanical engineering from Mahidol University, Nakhon Pathom, Thailand, in 1995, the master's degree in control engineering from Michigan Technological University, Houghton, MI, USA, in 1998, and the Ph.D. degree in robotics from Johns Hopkins University, Baltimore, MD, USA, in 2003. He established the Center for Biomedical and Robotics Technology (BART LAB), the first interdisciplinary research laboratory with the Faculty of Engineering, Mahidol University, in 2004. In 2006, he and his colleagues established the Department of Biomedical Engineering, Mahidol University, where he was the first BME Department Chair and remained, until 2015. From June 2015 to July 2023, he was the Dean of the Faculty of Engineering, Mahidol University. His research interests include medical robotics and field robotics, such as surgical robotics in various applications, rehabilitation robotics, hospital service and telemedicine robotics, and rough terrain rescue robotics. He was one of the founders of the Thai Robotics Society (TRS), in 2004, and the President, from 2007 to 2010. He also serves as a Trustee of the International RoboCup Federation and the Vice-President of RoboCup Asia-Pacific (RCAP). He is the Chair of the IEEE RAS Thailand Chapter.